Revista Internacional de Investigación e Innovación Tecnológica

Página principal: www.riiit.com.mx

Development of a low-cost integrated PWM controller and battery management system for a formula-type electric vehicle prototype

Desarrollo de un controlador PWM integrado de bajo costo y sistema de gestión de baterías para un prototipo de vehículo eléctrico tipo fórmula

López-Meraz, R.A.[a]*, Carmona-Valdés, J.C.[b], Méndez-Ramírez, C.T.[a], López-González, C.[c]

[a] Unidad de Ingeniería y Ciencias Químicas, Universidad Veracruzana, Xalapa, México, C.P. 91000. ORCID: https://orcid.org/0000-0002-3236-3709*, https://orcid.org/0009-0001-3877-1703.

[b] Universidad Nacional Autónoma de México, Av. Universidad 3004, 04510, Cd. De México, México. ORCID: https://orcid.org/0009-0008-8278-5193.

[c] Unidad de Ingeniería Universidad Veracruzana, Blvd. Adolfo Ruíz Corines No. 306, Poza Rica, México C.P. 93240. ORCID: https://orcid.org/0009-0002-2519-0114.

raullopez03@uv.mx*; julio.carmona0822@gmail.com; cmendez@uv.mx; carolinalog85@gmail.com

Technological innovation: Development of integrated controllers for electric vehicles.

Industrial application area: Electric mobility and sustainable transport systems.

Received: October 17, 2025
Accepted: August 24, 2026

Resumen

Este artículo presenta el diseño, implementación y validación experimental de un controlador integrado de bajo costo para un prototipo de vehículo eléctrico tipo fórmula. El sistema combina un módulo de control de velocidad basado en modulación por ancho de pulso (PWM) con un sistema de gestión de baterías (BMS) dentro de una arquitectura modular unificada, orientada a entornos académicos y de Formula SAE. El controlador, desarrollado con componentes comerciales accesibles, genera una señal sinusoidal de frecuencia variable mediante la comparación entre una referencia sinusoidal y una portadora triangular, que gobierna una etapa inversora con IGBTs. En paralelo, el BMS supervisa en tiempo real el voltaje, la corriente y la temperatura de un banco de 40 celdas Sony VTC6, incorporando funciones básicas de protección y balanceo pasivo. Los resultados experimentales muestran la generación estable de PWM para el accionamiento de un motor de 0.5 HP, así como una buena concordancia entre la corriente teórica, la medida por amperímetro y la obtenida con un sensor de efecto Hall, además de una respuesta térmica coherente durante una descarga de 1.5C. Se incluye una comparación funcional con controladores y BMS comerciales de referencia y se discute el alcance del prototipo como

plataforma de bajo costo para el desarrollo e integración de estrategias de control y supervisión en vehículos eléctricos tipo fórmula.

Palabras clave: Controlador PWM para motor eléctrico; Diseño modular de potencia; Gestión de baterías de ion-litio; Onda sinusoidal de frecuencia variable.

Abstract

This article presents the design, implementation, and experimental validation of a low-cost integrated controller for a formula-type electric vehicle prototype. The proposed system combines a PWM-based speed-control module with a battery management system (BMS) within a unified modular architecture intended for academic and Formula SAE environments. The controller, built from commercially available components, generates a variable-frequency sinusoidal waveform by comparing a sinusoidal reference with a triangular carrier, which drives an IGBT-based inverter stage. In parallel, the BMS monitors in real time the voltage, current, and temperature of a 40-cell Sony VTC6 lithium-ion battery pack, implementing basic protection and passive balancing functions. Experimental results demonstrate stable PWM generation for driving a 0.5 HP motor, good agreement between theoretical current, ammeter measurements and a Hall-effect sensor, and a consistent thermal response during a 1.5C discharge condition. A functional comparison with reference commercial controllers and BMS platforms is included, and the scope of the prototype is discussed as a low-cost platform for the integration of control and supervision strategies in formula-type electric vehicles.

Key words: PWM motor drive controller; Modular power electronics design; Lithium-ion battery management; Variable-frequency sinusoidal waveform.

I. Introduction

Formula vehicles are designed to achieve optimal performance in high-speed circuit tests, under strict safety and performance criteria defined by the Society of Automotive Engineers (SAE) for both dynamic and static events (Formula SAE, 2022). In a battery electric vehicle (BEV), the overall architecture can be understood through two main aspects: the power system and the dynamic analysis system, where the former is responsible for delivering the mechanical power demanded by the driving cycle and the latter studies the vehicle dynamics in motion (Patel et al., 2021). The power system typically comprises three main elements: the energy storage system, usually based on lithium-ion batteries; the energy management and control system; and the mechanical propulsion system, which generally includes an AC electric motor (Emadi *et al*., 2008; Nam, 2018; Patel *et al*., 2021). Within this structure, the controller is the essential element that connects the lithium batteries to the motor, acting as an inverter that transforms the DC power supplied by the accumulator into AC power while managing the operating point according to the driver's demand (UniTek Industrie Elektronik GmbH, 2012).

There are two widely used approaches to control traction motors in electric vehicles. The first focuses on directly managing the current supplied to the motor windings through vector control or similar advanced

strategies (Giri, 2013; Nam, 2018). The second relies on pulse-width modulation (PWM) in an electronic controller to regulate the frequency of the AC input and thus control the motor speed (UniTek Industrie Elektronik GmbH, 2012; Lu *et al*., 2011; Al-Ogaili *et al*., 2019; Brandstetter, P., 2012). Lu *et al*. (2011) show that induction-motor speed can be modulated using PWM strategies, while Al-Ogaili *et al*. (2019) employ sinusoidal PWM to improve charging efficiency. In addition, Birbir *et al*. (2019) designed a single-phase full-bridge inverter using PWM technology and a peripheral-interface microcontroller, achieving harmonic reduction through appropriate modulation. These works support the use of sinusoidal PWM as a practical and well-understood basis for variable-frequency motor drives in electric-vehicle applications. Complementing these contributions, recent reviews on harmonic behavior in inverter systems emphasize that waveform quality and harmonic content depend critically on the combination of modulation index, switching frequency, device characteristics and output filtering (Dewan and Straughen, 1975; Ghaderi et al., 2016; Khalid et al., 2019).

On the energy-storage side, most commercial traction controllers are optimized either for relatively low voltages and currents or for specific power levels, and only a limited number of solutions integrate detailed cell-monitoring capabilities in a single compact platform (Orion BMS, 2018; Victron Energy Blue Power, 2020). As a result, it is often difficult for university teams and low-budget projects to find affordable devices that combine traction control and battery supervision in a transparent and repairable way. At the same time, the literature on battery management systems (BMS) for electric vehicles highlights that, irrespective of architecture, every BMS must at least supervise cell voltage, charge and discharge current, and cell temperature, and must implement appropriate protection and balancing strategies (Manandhar *et al*., 2020; Krishna *et al*., 2024; Formula SAE, 2022). In a recent review, Ali *et al*., (2025) provide a comprehensive analysis of BMS technologies for electric vehicles, emphasizing thermal management, charging strategies and emerging functionalities as key factors in ensuring safety and extending battery life (Ali *et al*., 2025). Other surveys on energy and battery management for electric vehicles underline the need for coordinated strategies that integrate energy-flow control, state-of-charge estimation, and fault handling within a unified framework (Liu *et al*., 2022; Munsi & Chaoui, 2024). In parallel, specific works on racing and Formula-type applications discuss the requirements for robust, lightweight BMS architectures that can be integrated into compact accumulators for high-performance use (Bať a & Mikle, 2019).

In this context, the National Autonomous University of Mexico (UNAM), through the Faculty of Engineering and the UNAM Motorsports team, participates in the Formula SAE competition, which brings together around one hundred universities worldwide to design, build, and test formula-type electric vehicles under the international engineering standards proposed by SAE (Formula SAE, 2022; Enepaq, 2023). The design process must simultaneously consider the selected traction motor—in this case an EMBRAX 208 machine—and the characteristics of the available lithium-ion cells, such as the Sony/Murata VTC6 modules, whose electrical and thermal limits become the central pillar of both the controller and the BMS design (Enepaq, 2023; Davide, 2010; Victron Energy Blue Power, 2020). Although it is common to find both low-voltage and high-voltage controllers, these are not always designed to withstand discharge currents near 200 A or to expose a cell-level monitoring interface suitable for academic

experimentation. Therefore, developing a controller that not only regulates speed through PWM but also integrates cell-supervision capabilities represents a significant advantage for specialized mobility applications and for low-power converters coupled to cell-based storage systems (Emadi et al., 2008; Orion BMS, 2018; Ali et al., 2025).

Since the controller is a critical component in the vehicle design, two existing commercial units—the Bamocar D3 400-400 and the Sevcon Gen5 Size 9—were used as functional references to define target capabilities in terms of current, voltage, communication interfaces, and operating modes (BorgWarner, s.a.; UniTek Industrie Elektronik GmbH, 2012).

Table 1 summarizes the main characteristics of these two commercial controllers, which are not intended to be matched in every industrial feature, but rather to provide realistic reference values for current capability, voltage range, communication options and operating modes when defining the design objectives of the proposed prototype.

Table 1. Bamocar and Sevcon comparison.

Feature	Bamocar D3 400 400	Sevcon Gen5 Size 9
Manufacturer	Unitek	Sevcon
Controller Type	AC Motor / BLDC	AC Motor / BLDC
Maximum Output Current	400 A	550 A
Maximum Input Voltage	400 VDC	116 VDC
Maximum Power	Up to 150 kW (depending on version)	200 kW
Communication Interface	CAN, RS232	CAN, USB
Sensor Support	Resolver, Encoder	Resolver, Encoder
Operation Modes	Speed Control, Torque Control	Speed Control, Torque Control
Approximate Weight	9 kg	6 kg
Efficiency	~95%	~95%
IP Protection Rating	IP65	IP67
Common Applications	High-performance electric vehicles	Commercial electric vehicles
Operating Temperature	-20 °C to 85 °C	-40 °C to 85 °C
Switching Frequency	Programmable, up to 16 kHz	Programmable, up to 20 kHz
Size	More compact	More robust
Additional Features	Advanced vector control, regenerative braking	Multiple regenerative braking configurations

Likewise, the Orion 2 BMS and the N3-BMS from Lithium Balance were considered as conceptual references to identify the minimum supervision and protection functions required of a BMS in this context (Orion BMS, 2018). However, limitations in the availability of detailed technical information and hardware encouraged the development of an open, easy-to-repair architecture based on commercially accessible components, suitable for iterative prototyping within the UNAM Motorsports environment rather than for immediate industrial deployment (Emadi *et al*., 2008; Manandhar *et al*., 2020).

The article therefore focuses on the development and experimental validation of a low-cost, modular prototype capable of integrating motor-control and battery-monitoring functions within a common laboratory platform. The proposed system does not seek to reproduce the power capability, advanced control functions, environmental protection, reliability, or certification level of commercial traction

controllers and BMS platforms. Instead, its novelty lies in combining a sinusoidal PWM motor-control stage with cell-voltage, pack-current, and module-temperature monitoring, basic protection logic, and passive balancing in an open and repairable architecture tailored to a formula-type electric-vehicle prototype.

On the control side, the prototype implements a sinusoidal PWM strategy using an ATMEGA328P microcontroller, external memory, and high-speed comparators to generate the switching signals required by an IGBT-based power stage (Microchip, 2020; AG Electronics, 1998; Texas Instruments, 2014, 2023; Dewan & Straughen, 1975; Ghaderi *et al*., 2016). On the battery-management side, the BMS acquires and supervises cell voltages, pack current, and module temperatures using multiplexers, differential amplifiers, galvanic-isolation devices, and Hall-effect sensors, considering the safety requirements defined by Formula SAE (Formula SAE, 2022; Avago Technologies, 2020; Manandhar *et al*., 2020; Ali *et al*., 2025). The two subsystems remain conceptually separated and interact through alarm and protection signals.

Accordingly, the contribution of this work is not a fully vehicle-qualified traction controller, but an experimentally validated, transparent, and adaptable testbed for studying the functional interaction between PWM-based traction control, battery monitoring, protection strategies, and passive balancing. This low-cost platform is intended to support iterative prototyping, engineering education, and the development of subsequent control and supervisory strategies in Formula SAE and related electric-mobility applications (Emadi *et al*., 2008; Giri, 2013; Nam, 2018; Ali *et al*., 2025).

II. Materials and methods

2.1 Case study

The National Autonomous University of Mexico (UNAM), through the Faculty of Engineering and its UNAM Motorsports team, participates in the international Formula SAE competition, where more than one hundred universities develop and test electric formula-type vehicles under strict safety and performance regulations (Formula SAE, 2022). The design of the powertrain for the vehicle must simultaneously satisfy the competition rules, the characteristics of the selected motor and the limitations of the available energy-storage system. In this project, the system is based on an EMBRAX 208 AC motor and a lithium-ion battery pack assembled from Sony/Murata VTC6 cells, whose electrical, thermal and operating-current limits determine the main design criteria for both the controller and the battery management system (Enepaq, 2023; Davide, 2010; Victron Energy Blue Power, 2020). The project development was carried out following the process described in Figure 1. To design the elements of interest, in addition to considering the SAE regulations, it is necessary to consider both the EMBRAX 208 engine and the available cells.

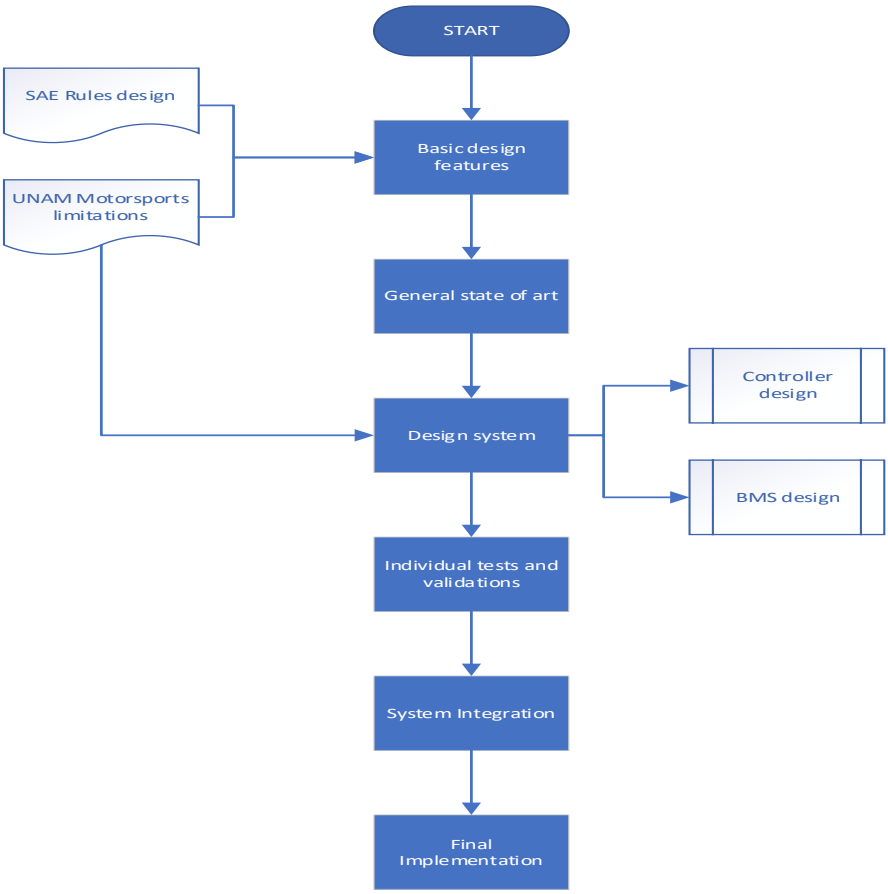


Figure 1. General design proposed for the implementation of the systems.

The accumulator used in the prototype tests is configured as an 80s8p arrangement of VTC6 cells, although for the purposes of controller and BMS validation a subset of 40 cells is employed to form a low-voltage battery with a nominal voltage of 14.4 V and a capacity of up to 31 Ah (Enepaq, 2023). The key parameters extracted from the VTC6 data sheet—such as nominal capacity, nominal voltage, maximum charge and discharge currents, and permissible temperature range—constitute the central pillar around which the proposed monitoring and protection strategy is defined (Enepaq, 2023; Davide, 2010). Table 2 summarizes these specifications and provides the reference envelope required to design both the PWM-based controller and the BMS measurement and protection circuits.

The laboratory tests reported in this study were conducted using a scaled-down 40-cell array to limit electrical risk and facilitate instrumentation during the initial validation phase. This reduced configuration was not intended to replicate the total voltage, stored energy, current capacity, thermal mass, or fault conditions of the final 80s8p battery pack. Instead, it was used to validate the operating principle of the BMS measurement chain—including voltage acquisition, pack current sensing, temperature monitoring, data logging, and basic protection logic—under laboratory conditions.

Therefore, the results obtained with the 40-cell array can be extrapolated to the complete battery pack only regarding the functional level of the monitoring architecture: the same measurement, protection, and balancing principles can be replicated for the full pack,

provided that the number of sensing channels, galvanic isolation requirements, voltage levels, wiring, protection devices, and thermal management provisions are appropriately scaled. The experimental results should not be interpreted as a direct validation of the complete 80s8p pack under vehicle operating conditions. Validation at the pack's final voltage and current ratings—including dynamic load testing and evaluation under fault conditions—remains necessary for vehicle-level implementation.

Table 2. Sony VTC6 Specifications.

Item			**Nominal**		**Note**
Nominal Capacity			3120mAh		Discharge at 0.2ltA, 2.0 V cutoff after Standard charge
Nominal Voltage			3.6V		
Charge Voltage			4.2V		
Energy Density			631Wh/l		
Item			**Rating**		**Note**
Rated Capacity			3000mAh		Discharge at 0.2ltA, 2.0V cutoff after Standard charge
Maximum Charge Voltage			4.25V		
Cutoff Voltage			2V		
Continuous Maximum Charge Current			5A 6A		Continuous Pulse
Continuous Maximum Discharge Current			30A 15A		With 80 deg temperature cut Without 80 deg temperature cut
Allowable Environment Temperature		Charge	0 – 60°C		Refer to the cell temperature spec of 2.8 for cell surface temperature
		Discharge	-20 – 60°C		
Weight			46.6 ± 1.5 g		
Temperature Range / Cell Surface Temperature Range			**Upper Limited Charging Voltage**	**Maximum Charging Current**	**Charging Current Recommendation**
1	Low Charging Temperature Range	0°C≤T<10°C	A	4.25V	2A	1A
			B	4.15V	4A	2A
2	Standard Charging Temperature Range	10°C≤T≤45°C		4.25V	5A	3A
3	High Charging Temperature Range	45°C<T≤60°C		4.20V	5A	2A

The above information defines the central design constraints for both the controller and the BMS. In practice, while low- and high-voltage commercial controllers are widely available, they are not conceived to operate close to the 200 A discharge levels required by the target application, nor to expose an open cell-monitoring interface suitable for academic experimentation. For this reason, the initial development of the present prototype treated the controller and the BMS as two parallel subsystems, linked only through alarm and protection signals,

with the explicit aim of later integrating them into a single modular architecture.

2.2 Fundamentals and principles

Even when two electronic subsystems are intended to be integrated into a single physical platform, it is essential to develop them separately at the conceptual level before defining their coupling strategy. For this reason, the proposed system is decomposed into a controller block and a BMS block. The operating principle of the controller is based on PWM theory to generate a sinusoidal waveform of variable frequency from a DC source, whereas the BMS focuses on the acquisition and supervision of cell-level and pack-level variables that determine the safe operating area of the accumulator (Dewan and Straughen, 1975; Emadi *et al*., 2008).

From the controller perspective, the traction-drive function is implemented as a single-phase inverter whose switches are driven by PWM signals obtained from the comparison between a sinusoidal reference and a triangular carrier. This approach is consistent with classical PWM techniques and with the implementation commonly found in commercial controllers such as the Bamocar family, where dedicated hardware generates both the triangular and sinusoidal waveforms and compares them to obtain the switching pattern (Dewan and Straughen, 1975; UniTek Industrie Elektronik GmbH, 2012). The modulation strategy is defined by the frequency index $m_f = {}^{F_c}/_{F_r}$, which must be greater than 21 to avoid the excessive growth of harmonic components in low-order periods, and by the modulation index $m_a = {}^{A_r}/_{A_c}$, which relates the amplitudes of the reference and carrier signals and is used to adjust the output-voltage level (Dewan and Straughen, 1975; Ghaderi *et al*., 2016). A proper selection of m_f, m_a and the output filter is fundamental to obtain a waveform that approximates the desired sinusoidal output while keeping harmonic distortion within acceptable limits (Ghaderi *et al*., 2016; Palmas-Peláez and García-Vite, 2013).

From the BMS point of view, the operating principle is oriented toward the safe management of the lithium-ion battery pack used in the vehicle. The literature on electric-vehicle BMS consistently identifies cell voltage, pack and segment currents, and cell or module temperature as the core variables that must be monitored to prevent overcharge, over-discharge, overcurrent and thermal runaway (Manandhar *et al*., 2020; Ali *et al*., 2025). In addition, Formula SAE regulations explicitly require that at least 80% of the cells be monitored in terms of temperature and that the accumulator be equipped with adequate provisions for current interruption in case of fault (Formula SAE, 2022). Commercial platforms such as the Orion 2 BMS implement these requirements using multiplexer-based voltage measurement, isolated differential amplifiers and microcontroller-based processing, which serve as a conceptual reference for the present design (Orion BMS, 2018; Victron Energy Blue Power, 2020).

2.2.1 Control area

The most important function of the control area is the generation of PWM pulses that will drive the power switches of the inverter. According to PWM theory, there are two implementation-friendly methods for generating such pulses. The first, known as digital partitioning, relies on a microcontroller that creates a base frequency and then distributes time slots among the different outputs. The second, adopted in this work, consists of comparing two analog signals: a sinusoidal reference and a triangular carrier whose frequency satisfies the condition $m_f > 21$ (Dewan and Straughen, 1975). Figure 2 illustrates this method,

showing the comparison of the reference and carrier signals using a high-speed operational-amplifier comparator and the resulting PWM signal (Dewan and Straughen, 1975).

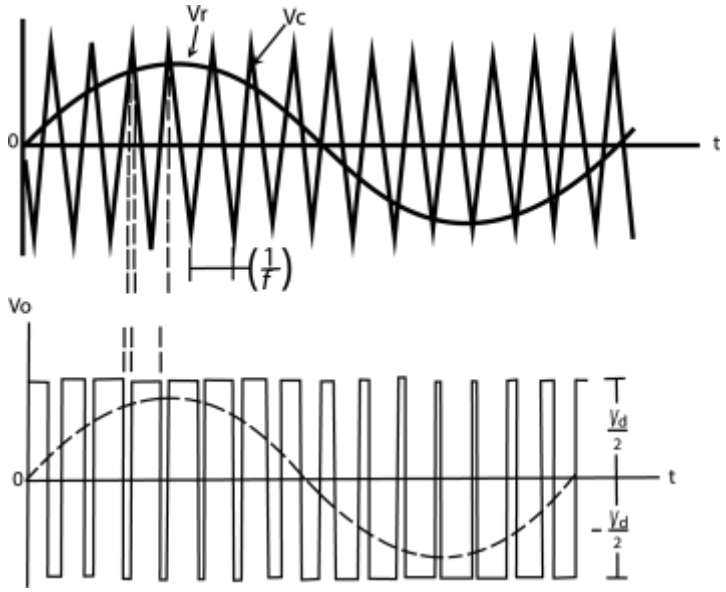


Figure 2. Representation of signal comparison using a high-speed operational amplifier for pulse generation (a) Reference and control signals (b) Voltage Va, PWM pulses (Dewan and Straughen, 1975).

In the proposed prototype, the ATMEGA328P microcontroller is used together with an external EEPROM to generate both the sinusoidal and triangular waveforms (Microchip, 2020; AG Electronics, 1998). A list of hexadecimal values corresponding to discretized samples of the reference and carrier signals is stored in the memory; these values are then sequentially read and converted into analog voltages by the digital-to-analog converter associated with the microcontroller. The sampling rate of the memory is controlled by an NE555 timer, whose configuration includes a variable resistor that can be linked to the accelerator pedal through a Wheatstone-bridge arrangement, allowing the effective PWM frequency to change as a function of the driver demand (Texas Instruments, 2014; Dewan and Straughen, 1975).

To perform the comparison between the reference and carrier signals, two OPA814 high-speed operational amplifiers are used in comparator mode, considering that the device can handle comparison frequencies up to hundreds of megahertz (Texas Instruments, 2023). One amplifier compares the triangular signal with the sinusoidal waveform at phase 0°, while the second compares the triangular signal with the sinusoidal waveform shifted by 180°. This arrangement allows the system to obtain two complementary PWM signals without requiring the amplifier to process negative voltages. Figure 3 shows the schematic diagram of the generation of both carrier and reference waves from the EEPROM and DAC, and Figure 4 presents the resulting PWM waveforms corresponding to the two phases and their unified output (Dewan and Straughen, 1975; UniTek Industrie Elektronik GmbH, 2012).

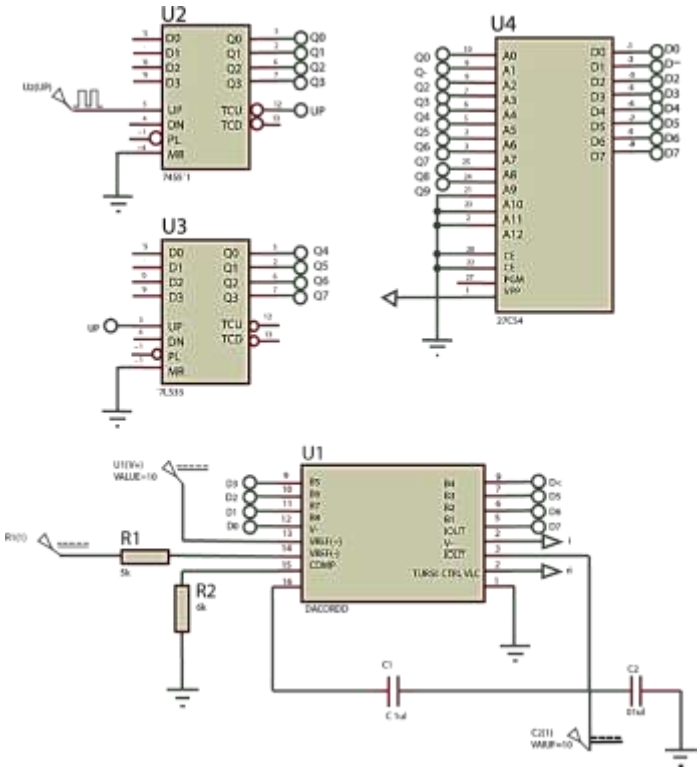


Figure 3. Schematic diagram of the generation of both carrier and reference waves from the reading of a 27C64 EEPROM memory and a DAC digital-to-analog converter.

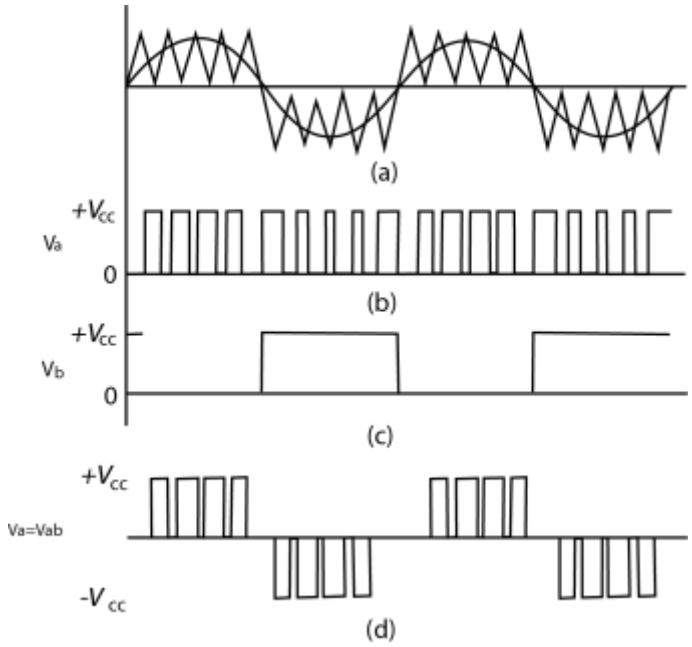


Figure 4. Generation of the PWM signal for the odd and even switches is done from two different phases of the sine wave. (a) First positive half cycle of phase 0 and the negative half cycle of phase 180, these phases are compared with the generated triangular signal. (b) The voltage Va represents the initial comparison between the sine wave in phase 0 and the triangular signal. (c) The output voltage Vb represents the comparison during the negative half cycle of phase 180. (d) Unified PWM signal Va-Vb.

2.2.2 Power zone

The power zone is responsible for converting the PWM control signals into the high-current, high-voltage output required to drive the motor. In a PWM inverter, this stage is mainly composed of semiconductor switches that open and close at the PWM frequency to synthesize the desired output waveform (Dewan and Straughen, 1975; Ghaderi *et al*., 2016). The choice of switching device depends on the voltage and current levels to be handled, as well as on switching-speed requirements and thermal constraints. Although TRIACs and thyristors are widely used in power systems due to their bidirectional conduction capability and robustness, their relatively slow switching speed can introduce significant waveform distortion in PWM applications, especially in systems where regenerative braking or high switching frequencies are required (Ghaderi *et al*., 2016; Emadi *et al*., 2008).

Given the expected operating current—around 96 A for the target track and vehicle configuration, as estimated by the UNAM Motorsports team using energy-based calculations of the required mechanical work—and the required switching frequency, the design adopts IGBT transistors as the main switching devices (Emadi *et al*., 2008; Mouser Electronics, 2020). Specifically, the FGH60N60SFD model is selected because it combines adequate current-carrying capacity, high switching speed and local market availability (Mouser Electronics, 2020). Figure 5 shows the connection of the IGBTs, the motor and the 336 V accumulator, highlighting the power section components and their relation to the control and BMS subsystems.

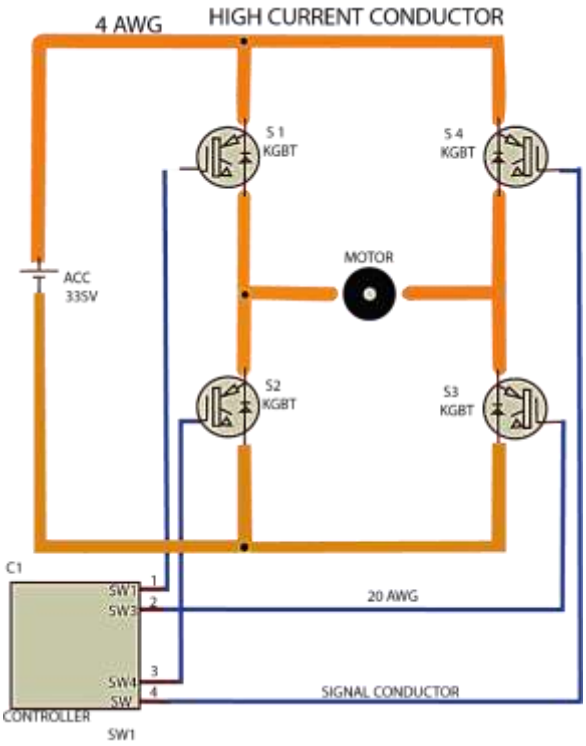


Figure 5. Representation of the power section with the assigned IGBTs and the connection to the motor and the 336 V accumulator. The components connected to the orange wire represent the power section.

To protect the IGBTs and limit current surges associated with switching events, a filtering and current-limiting stage based on inductors is included in the power zone (Ghaderi *et al*., 2016). The inductors are designed to saturate at around 100 A, slightly above the estimated nominal current, so that they can effectively limit transient current spikes without unduly restricting steady-state operation. Proper selection of the inductance value and saturation current is essential, since these parameters influence both the dynamic behavior of the inverter and the harmonic content of the output waveform (Ghaderi *et al*., 2016).

2.2.3 BMS Measurements

The design of the BMS begins with the definition of the accumulator architecture and the selection of the cells, as these choices determine the voltage and energy capacity of

the packas well as the critical variables that must be monitored (Patel et al., 2021). For the UME-23 vehicle, the accumulator employs an 80s8p configuration of VTC6 cells, but the prototype discussed in this article uses 40 cells for laboratory-scale testing (Enepaq, 2023). According to Formula SAE rules and general BMS practice, the variables that must be monitored as a minimum are cell voltage, charge and discharge current, and cell temperature, with at least 80% of the cells covered by the temperature-measurement system (Formula SAE, 2022; Ali et al., 2025).

Direct measurement of every individual cell voltage using separate ADC channels would require a microcontroller with an impractically large number of analog inputs and would hinder efforts to keep the system compact and low-cost. For this reason, the proposed BMS adopts a multiplexed measurement strategy like that used in commercial systems such as the Orion 2 BMS, where a sequential multiplexer connects groups of cells to a differential amplifier that calculates their individual voltages (Orion BMS, 2018; Victron Energy Blue Power, 2020). In the present design, an ADG507A 8×2 multiplexer is used to measure up to four cells at a time, together with a THS4561IDGKT differential amplifier that processes the voltage difference between two nodes corresponding to the multiplexer outputs. Figure 6 depicts the connection scheme used to obtain cell-voltage data and the capacitive isolation network required to preserve system integrity, while Figure 7 illustrates typical correct and incorrect multiplexer connections, highlighting the importance of maintaining proper ordering of the input pins.

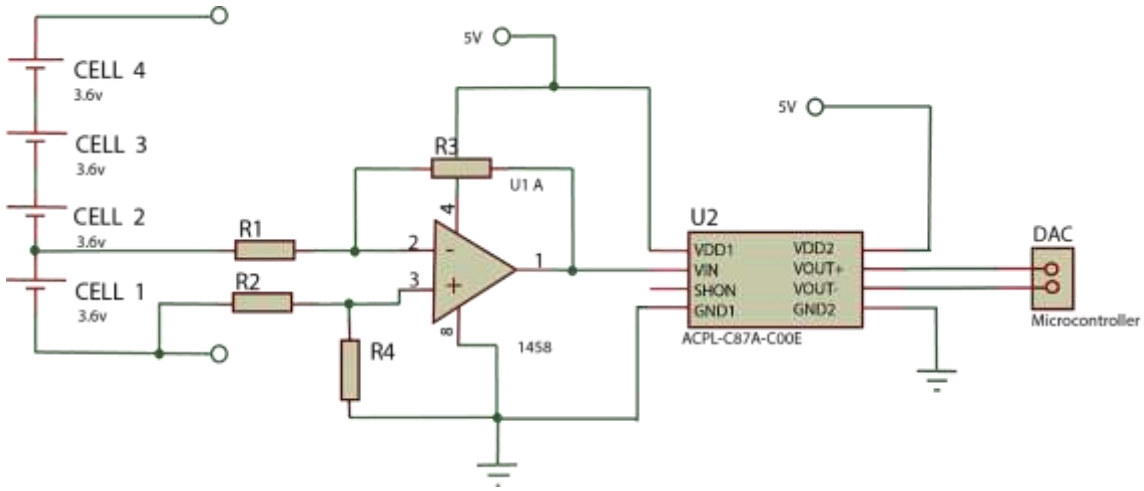


Figure 6. Connection schematic designed to obtain cell voltage data, along with the necessary capacitive isolation to ensure system integrity.

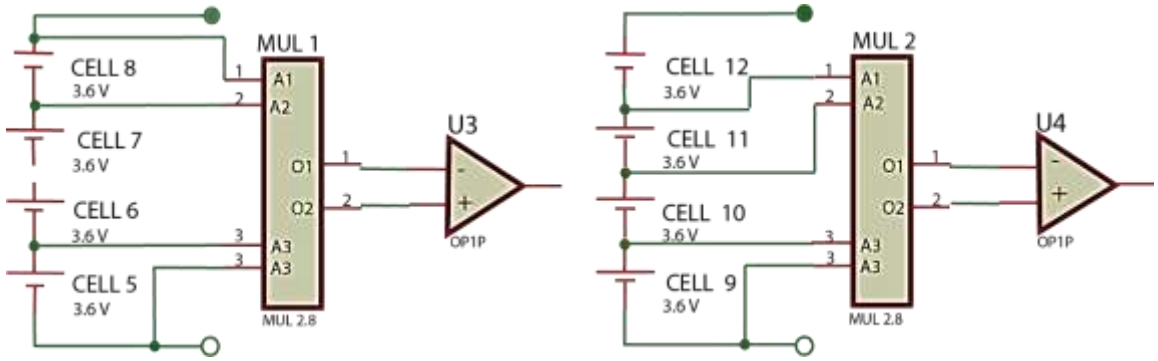


Figure 7. Schematic of the incorrect connection of input pins to the multiplexer with the cells (far left) and one with a correct connection (far right).

To ensure galvanic isolation between the high-voltage battery domain and the low-voltage measurement and control circuits, the differential-amplifier outputs are coupled to the microcontroller through ACPL-C87A isolation devices (Avago Technologies, 2020). This arrangement allows the microcontroller to safely monitor the cell voltages while respecting the creepage and clearance distances mandated by Formula SAE and general safety practices (Formula SAE, 2022; Avago Technologies, 2020). Because monitoring 80 cells requires a significant number of analog channels, the design combines the internal ADC pins of an ATMEGA328P with external ADC expansion as needed, ensuring that every cell in the series string can be measured within the required update interval (Microchip, 2020).

Discharge-current measurement can be implemented either at the level of individual cells or modules or at the total pack output (Emadi *et al.*, 2008). Although per-cell or per-module measurement provides more granular control and enables selective disconnection of sections in case of overcurrent, it also increases sensor count, wiring complexity, cost and mass. For the present prototype, a simpler architecture is adopted: a single Hall-effect current sensor located at the output of the accumulator measures the total discharge current and triggers a cut-off mechanism if the current exceeds the allowable limit, thereby protecting both the cells and the driver (Emadi *et al.*, 2008). The selected model, ACS758LCB-050B-PFF-T, offers adequate current range for the experimental setup and is readily available on the local market.

In terms of charge-current measurement and balancing, several techniques can be found in the literature, including cell disconnection and reconnection, cell bypass and charge-current adjustment using external power converters (Victron Energy Blue Power, 2020; Davide, 2010). The present design opts for a relatively simple current-bypass balancing approach, in which each parallel branch can be shunted by a resistor and an electronic relay once the corresponding cell voltage reaches a predefined threshold (Davide, 2010). Figure 8 shows the balancing circuit employed, where the Panasonic AQY282S solid-state relay and a resistor form a bypass path that limits the balancing current to approximately 100 mA, in line with recommendations for typical lithium-ion applications (Davide, 2010).

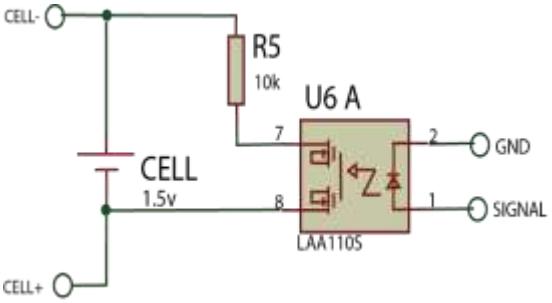


Figure 8. Balance circuit.

For temperature measurement, the UME-23 project takes advantage of the temperature sensors already integrated in the Enepaq VTC6 modules (Enepaq, 2023). The differential-voltage signal from these sensors is extracted through the J11 connectors specified by the manufacturer and conditioned so that it can be acquired by the BMS microcontroller. In accordance with Formula SAE requirements, the BMS is configured so that an over-temperature condition detected in the monitored cells can lead to an accumulator isolation relay (AIR) opening event, interrupting the current flow and protecting the system (Formula SAE, 2022).

Once voltage, current and temperature measurements are acquired, they are processed by the microcontroller and stored on an SD card for subsequent analysis. Communication between the measurement microcontroller and a second microcontroller dedicated to data logging is implemented via TXD and RXD serial lines, and the SD-card expansion module is connected as shown in Figure 9 (Manandhar *et al.*, 2020). This arrangement allows the system to record large numbers of measurements during discharge tests and to perform off-line analysis of cell behavior, current profiles and thermal response, which is essential for validating the prototype and for refining the design of future iterations.

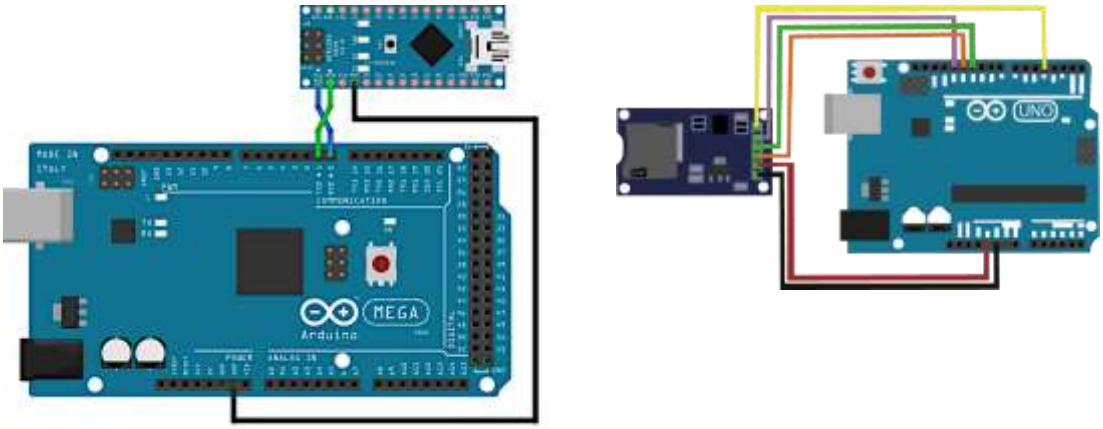


Figure 9. Microcontroller connection for communication and data storage.

III. Results

The results are divided into two main subsections. The first one corresponds to the controller and focuses on the generation of PWM pulses and their ability to drive a single-phase inverter for motor-speed control. The second one presents the performance of the BMS, emphasizing voltage, current and temperature measurements and their consistency with the expected behavior of the lithium-ion cells used in the prototype.

3.1 Controller

The implementation of the controller was evaluated from two complementary perspectives. First, the quality and behavior of the PWM signals generated in the control area were analyzed as the effective switching frequency was varied according to the driver

demand. Second, the ability of the power stage to supply current to a 0.5 HP motor while adjusting its speed was assessed under laboratory conditions.

To examine PWM generation, an oscilloscope was connected at the output of the comparator stage, and the input resistance associated with the accelerator pedal was adjusted to emulate different driver demands. As described in Section 2.2.1, the PWM signal is obtained by comparing a sinusoidal reference and a triangular carrier whose frequency is determined by the NE555-controlled sampling of the EEPROM data (Dewan & Straughen, 1975; Texas Instruments, 2014; Microchip, 2020; AG Electronics, 1998). Figure 10 illustrates the PWM signal generated in a positive cycle. Negative cycles are attenuated because the amplifier cannot reproduce negative voltages.

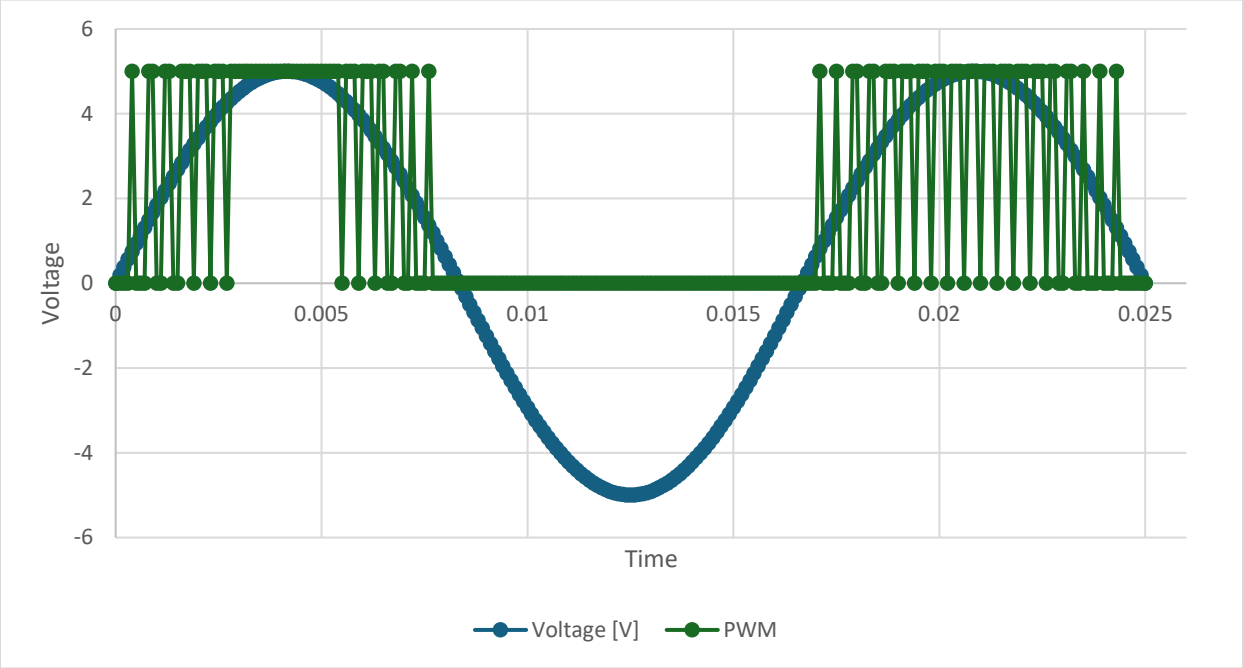


Figure 10. The carrier signal is shown along with the train of PWM pulses generated from it. The carrier is offset by 5 V to allow visualization of both the input and output signals.

Figure 10 illustrates the PWM signal corresponding to a positive half-cycle of the sinusoidal reference. In this configuration, the carrier signal is represented in blue and shifted by 5 V so that the comparison between input and output can be observed on a single oscilloscope screen. At an output frequency of 60 Hz, the PWM pattern comprises approximately ten pulses per cycle, as determined during the ATMEGA-based tests. Although this number of pulses is not sufficient to generate a highly refined sine wave, it is adequate for achieving the nominal motor speed of 1500 rpm and demonstrates the feasibility of the proposed PWM generation scheme using low-cost hardware.

Given that the available experimental setup lacked a power quality analyzer or instrumentation capable of directly measuring total harmonic distortion (THD) or performing spectral analysis, Figure 11 is included solely as an analytical and illustrative representation of the operating principle of sinusoidal pulse-width modulation (SPWM).

The figure was constructed based on the control principle implemented in the prototype, wherein a sinusoidal reference signal is compared with a triangular carrier signal to generate the switching pulses that drive the inverter stage. The first panel depicts idealized reference and carrier signals; the second shows the idealized PWM switching pattern resulting from their comparison; and the third qualitatively illustrates the expected effect of the output filtering stage—namely, the attenuation of high-frequency switching components and the resulting signal's tendency toward the sinusoidal fundamental component at the motor terminals. This representation follows the classical principles of sinusoidal PWM modulation described in power electronics literature (Dewan and Straughen, 1975) and aligns with the use of PWM switching strategies in electric drive applications (Ghaderi *et al*., 2016; Emadi *et al*., 2008).

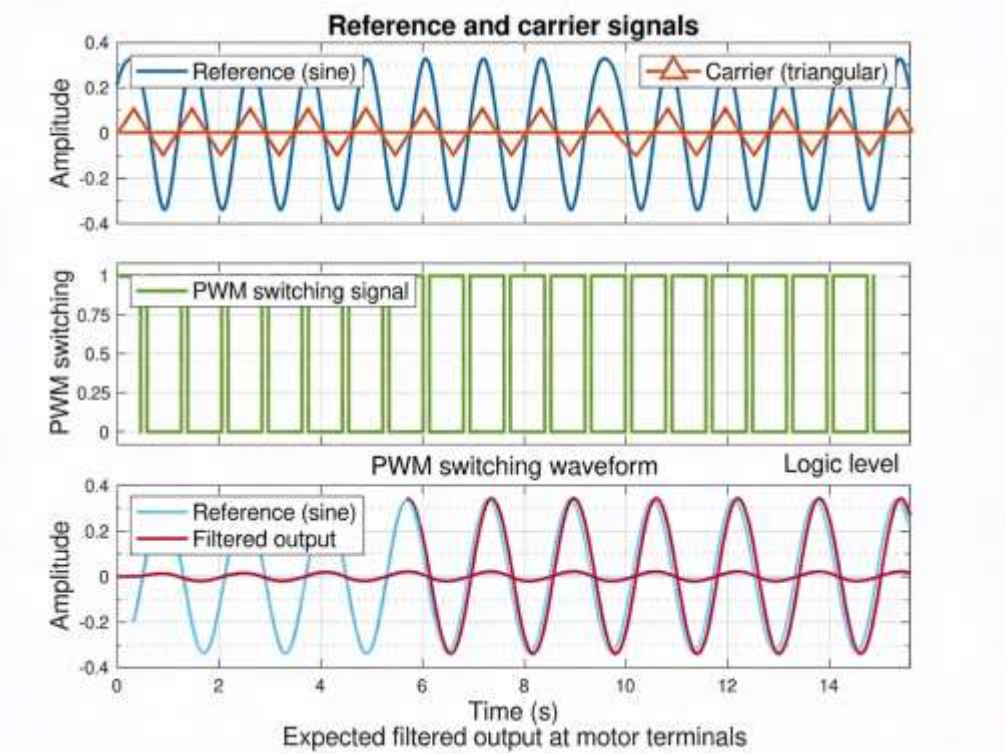


Figure 11. Analytical and illustrative representation of the sinusoidal PWM generation principle and the expected qualitative effect of output filtering. The first panel shows the sinusoidal reference signal and the triangular carrier used to generate PWM; the second illustrates the idealized PWM switching pattern resulting from their comparison; and the third represents the qualitative trend of the filtered output signal toward the sinusoidal fundamental component at the motor terminals.

Consequently, Figure 11 is limited to facilitating the physical interpretation of the PWM pulses experimentally observed in Figure 10 and to explaining, based on classical SPWM theory, that the harmonic components associated with switching are concentrated around the carrier frequency and its sidebands. Quantitative harmonic characterization—including direct THD measurement and spectral analysis under representative load conditions—is identified as future work.

From the power-stage perspective, the inverter based on FGH60N60SFD IGBTs was able to supply the current required by the 0.5 HP motor under the tested laboratory conditions. The inductive filtering stage,

designed to saturate at approximately 100 A, was intended to limit transient current surges during switching events and to contribute to the protection of the IGBTs; however, its transient performance was not quantitatively characterized in the present experimental campaign (Mouser Electronics, 2020; Ghaderi *et al.*, 2016). Although the experimental program did not include a full efficiency characterization, the observed operation indicates that the selected switching devices and filter configuration are suitable for the current levels tested in the laboratory setup. Their performance at the final voltage and current ratings of the target application requires further validation.

3.2 BMS

When evaluating the BMS, several critical aspects must be considered to ensure that voltage, current and temperature are measured accurately and that the resulting information is useful for both protection and post-test analysis. The experimental validation focuses on three main elements: the response of the voltage-measurement circuit to intentional disconnection events, the consistency of the current-measurement subsystem, and the thermal behavior of the monitored module under a 1.5C discharge condition.

For voltage-measurement tests, the BMS was connected to a sample arrangement of the storage system based on the UME-23 module architecture. Figure 12 shows the connection of the module to the main accumulator relays. At a certain point during testing, this connection was intentionally interrupted to verify whether the BMS could detect the fault and open the accumulator isolation relay (AIR) as required by safety regulations (Formula SAE, 2022). Figure 12 shows the connection of the cells of the storage system.

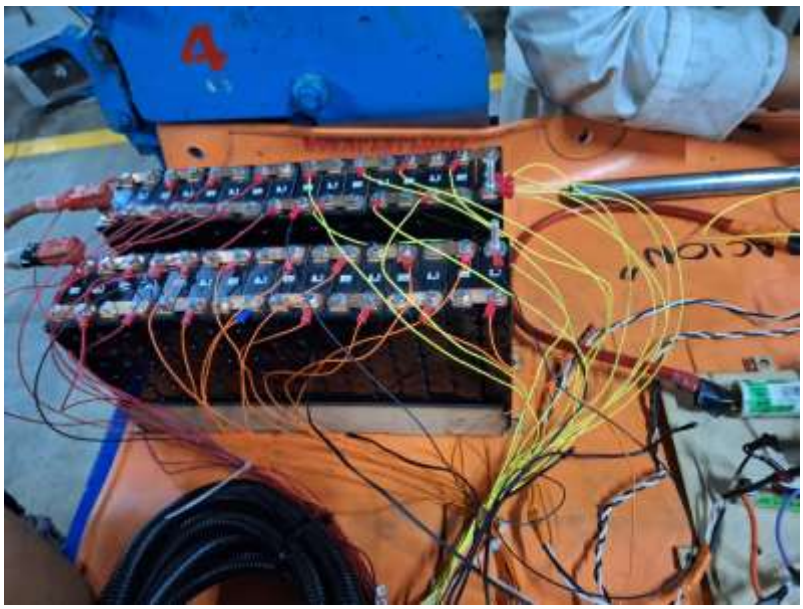


Figure 12. Sample connection of a complete module to the general relays of the storage system. The BMS monitors the module voltages and can trigger the opening of the AIR in case of fault.

The BMS successfully detected the interruption and commanded the opening of the AIR, confirming the correct operation of the voltage-measurement and fault-detection chain under the tested conditions. Due to the limited capacity of the prototype BMS board, tests were carried out with a reduced number of cells, but the measurement principle remains the same for the complete 80s8p configuration.

For current-measurement validation, the prototype used a resistive-load test derived from the low-voltage 40-cell accumulator. Three resistances (180 Ω, 5 Ω and 1 Ω) were selected to generate different current levels, and for each case the theoretical current, the current measured by a reference ammeter, and the current reported by the Hall-effect sensor (ACS758LCB-050B-PFF-T) were recorded (Emadi *et al*., 2008; MOUSER ELECTRONICS, 2020). These results are summarized in Table 3.

Table 3. Comparison of theoretical current, ammeter reading, and Hall-sensor measurement for different resistive loads.

180 Ohm		
Theoretical	**Ammperemeter**	**Hall sensor**
0.07	0.1	0.06
0.07	0.1	0.06
0.07	0.1	0.06
5 Ohm		
Theoretical	**Ammperemeter**	**Hall sensor**
2.4	2.5	2.42
2.4	2.6	2.42
2.4	2.5	2.42
1 Ohm		
Theoretical	**Ammperemeter**	**Hall sensor**
12	12.1	12.05
12	12.1	12.05
12	12.2	12.05

Figure 13 emphasizes the strong agreement between the theoretical current values and the experimental measurements obtained from both the ammeter and the Hall-effect sensor for the three resistive loads. As the resistance increases from 1 Ω to 5 Ω and 180 Ω, the current magnitude decreases by more than one order of magnitude, which is consistent with the expected behavior and supports the validity of the proposed model. This graphical summary therefore clarifies the trend already reported in Table 3 and provides a more intuitive visual representation.

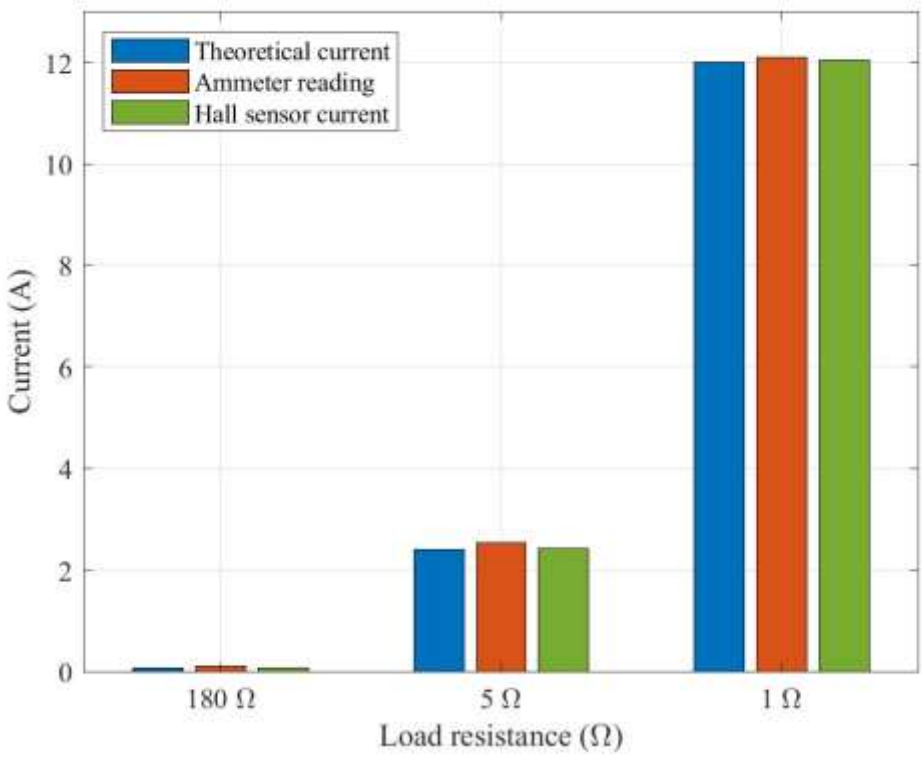


Figure 13. Comparison of theoretical current, ammeter reading, and Hall-sensor measurement for resistive loads of 180 Ω, 5 Ω and 1 Ω.

Overall, the comparison among theoretical values, ammeter readings, and Hall-effect sensor measurements supports the internal consistency of the experimental setup and the suitability of the measurement scheme for the initial validation of the prototype. For representative current conditions—loads of 5 Ω and 1 Ω—the Hall-effect sensor exhibited relative deviations from the theoretical values of approximately 0.8% and 0.4%, respectively. In contrast, for the 180 Ω load, the absolute difference of 0.01 A is more informative because the low current magnitude amplifies the relative error.

Previous experimental studies have utilized resistive and inductive loads to characterize SPWM inverters and have demonstrated the utility of comparing measured electrical variables against the theoretical or simulated behavior of the converter (Aihsan, *et al*., 2020; Kamal & Al-Fattah, 2025). Furthermore, the use of Hall-effect current sensors—including the ACS758—for current acquisition in experimental inverter setups has been documented, supporting their application as an isolated measurement alternative in power electronics systems (Tamrakar, *et al*., 2023).

Figure 13 shows that the Hall-effect sensor closely follows both the theoretical current and the ammeter reading across the three test points. The agreement is particularly strong at the moderate and high current levels associated with the 5 Ω and 1 Ω loads, which supports the suitability of the selected Hall sensor as a low-cost current-monitoring device in the integrated BMS architecture (Emadi *et al*., 2008).

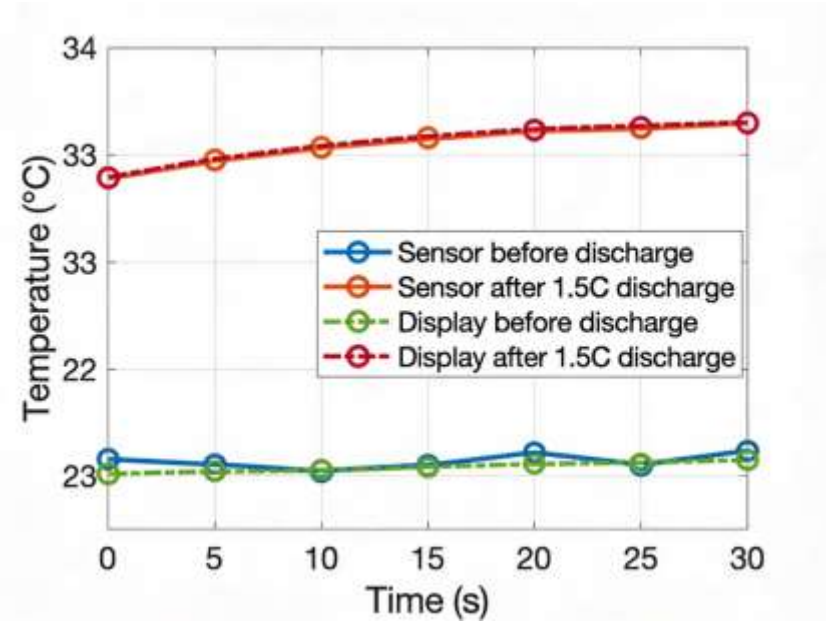


Figure 14. Temporal evolution of temperature before discharge and after the 1.5C discharge condition, showing both the display-based readings and the sensor-based measurements.

The thermal behavior of the monitored module was evaluated by comparing the temperature readings obtained before discharge with those measured after a 1.5C discharge condition. These data are summarized in Table 4, which reports both the values shown on the module display and the temperatures recorded by the sensors connected to the BMS.

Table 4. Temperature readings before discharge and after a 1.5C discharge condition, obtained from the module display and the BMS sensors.

	Before discharge		**After discharge 1.5C (120s)**	
Data time	**Display temp.**	**Sensor temp.**	**Display temp.**	**Sensor temp.**
0	23	23.2	32	32.4
5	23	23.4	33	32.7
10	23	23.5	33	32.8
15	24	23.7	32	32.8
20	23	23.2	34	33.2

25	23	23.2	33	33.1
30	23	23.5	33	33.4

The temperature data from Table 4 are digitized and represented as a time series to make the evolution of the thermal variables more explicit.

Figure 14 indicates that both measurement sources follow a consistent trend and that the thermal rise associated with the 1.5C discharge condition is clearly detectable by the BMS. The maximum temperatures remain within the allowable range specified in the VTC6 data sheet for the tested conditions, and the BMS would have been able to trigger a protection event if the temperature had approached unsafe limits (Enepaq, 2023; Davide, 2010; Victron Energy Blue Power, 2020).

Overall, the experimental results show that the sinusoidal PWM strategy implemented with commercially accessible hardware can provide an appropriate actuation signal for the traction motor, achieving the expected current levels for the tested resistive loads. In parallel, the BMS architecture proves capable of reliably measuring and processing the key electrical and thermal variables of the battery pack under laboratory-scale operating conditions, consistent with the monitoring and protection functions reported in the literature and with the relevant safety-oriented requirements for electric-vehicle applications (Formula SAE, 2022; Emadi et al., 2008; Ali et al., 2025).

The maximum temperature rise following the 1.5C discharge was approximately 10°C relative to the initial condition, remaining within the range specified in the VTC6 cell datasheet for continuous discharge operation. This quantitative thermal behavior confirms that, under the laboratory conditions employed, the module operates within a safe zone, maintaining sufficient margins relative to the over-temperature limits established by the manufacturer.

These results should be interpreted within the functional scope of the laboratory prototype rather than as a direct performance comparison with commercial traction controllers or industrial BMS platforms. As summarized in Table 1, commercial controllers such as the Bamocar D3 400/400 and Sevcon Gen5 Size 9 are designed for substantially higher voltage, current, and power levels and incorporate advanced features such as robust communication interfaces, motor-feedback support, regenerative-braking options, environmental protection, and vehicle-oriented reliability functions.

In contrast, the present prototype was evaluated using a 0.5 HP motor and a reduced battery arrangement under laboratory-scale conditions. Its contribution is not to match commercial products in power capability, efficiency, environmental protection, reliability, or certification, but to provide a modular and repairable experimental platform in which PWM-based motor control, cell-voltage monitoring, pack-current sensing, temperature monitoring, alarm logic, and basic protection functions can be studied together. Accordingly, the results demonstrate functional feasibility at laboratory scale and establish a basis for subsequent validation under the voltage, current, thermal, dynamic-load, and safety conditions required for vehicle-level implementation.

IV. Conclusion

This work presented the design, implementation, and laboratory validation of a low-cost single-phase inverter with sinusoidal PWM speed regulation and an integrated BMS for a formula-type electric vehicle. The proposed controller, built from readily available components, was able to generate an appropriate actuation signal for the traction motor, achieving current levels and waveforms that are consistent with the theoretical model for the tested resistive loads.

The additional current-comparison analysis confirmed a close agreement between the theoretical values and the measurements obtained from both the ammeter and the Hall-effect sensor, which supports the correctness of the sizing and the adequacy of the control strategy. This comparison also clarifies the relationship between load resistance and current magnitude, providing a more transparent link between the design assumptions and the experimental results.

Regarding the energy-storage system, the developed BMS architecture proved capable of monitoring the key electrical and thermal variables of the battery pack under laboratory-scale operating conditions. The temperature measurements obtained from the dedicated sensors and from the module display showed a consistent thermal evolution before and after the 1.5C discharge test, indicating that the proposed measurement chain is reliable for detecting relevant temperature variations.

From a safety and standards perspective, the experimental validation indicates that the proposed controller–BMS integration satisfies the key measurement, protection, and monitoring requirements typically considered in electric-vehicle applications, such as those in Formula SAE regulations. In addition, the prototype provides a practical platform for studying inverter control, battery-pack monitoring, and safety-oriented design in electric-mobility systems, and it establishes a basis for future developments toward more advanced implementations

Future work will focus on extending the validation to dynamic driving cycles closer to real track conditions, refining the harmonic characterization of the output waveform through direct THD and spectral measurements, integrating onboard communication and data-logging capabilities, and developing a validated MATLAB/Simulink model to assess harmonic behavior, efficiency, and system response under representative operating conditions.

From an industrial implementation perspective, the presented prototype is not intended to replace the commercial traction controllers and BMS units used in production electric vehicles or established racing equipment. Its main limitations regarding industrial implementation include the absence of formal certifications, validation restricted to laboratory tests with static loads, the lack of dynamic driving cycle testing, and the omission of advanced diagnostic strategies and high-level CAN communication. However, the proposed modular architecture replicates the key functional blocks of a real traction system—PWM inverter, cell-level monitoring, balancing, and thermal protection—using readily available components. This makes it a suitable foundation for future iterations to incorporate communication modules, vector control strategies, and robustness checks that bring the design closer to meeting industrial product requirements.

From an electrical-safety perspective, the laboratory prototype incorporates galvanic

isolation between the battery measurement domain and the low-voltage control electronics, together with voltage, current, and temperature monitoring. The protection logic is designed to command accumulator isolation through the AIR when a monitored variable reaches its configured threshold. These features provide a safety-oriented basis for laboratory operation; however, they do not constitute verification of compliance with automotive functional-safety, insulation-coordination, electromagnetic-compatibility, or vehicle-level fault-tolerance requirements.

V. References

AG Electronics. (1998). *AM27C64 CMOS EPROM* [Data sheet]. https://agelectronica.lat/pdfs/textos/A/AM27C64.pdf

Aihsan, M. Z., Yusof, A. M., Ahmad, N. I., Saifizi, M., Habibah, H. M., Rahman, D. H. A., & Mustafa, W. A. (2020). Performance analysis of unipolar SPWM inverter: Resistive load and inductive load. *IOP Conference Series: Materials Science and Engineering*, *932*(1), Article 012074. https://doi.org/10.1088/1757-899X/932/1/012074

Ali, A. O., Abdelrehim, O., Saafan, M. M., Elmarghany, M. R., & Hamed, A. M. (2025). Comprehensive review of battery management systems for electric vehicles: Thermal management, charging strategies, and emerging technologies. *Journal of Power Sources*, *658*, Article 238269. https://doi.org/10.1016/j.jpowsour.2025.238269

Al-Ogaili, A., Aris, I., Verayiah, R., Ramasamy, A., Marsadek, M., Rahmat, N. A., Hoon, Y., Aljanad, A., & Al-Masri, A. N. (2019). A three-level universal electric vehicle charger based on voltage-oriented control and pulse-width modulation. *Energies*, *12*(12), Article 2375. https://doi.org/10.3390/en12122375

Avago Technologies. (2020). *ACPL-C87A precision optically isolated voltage sensor* [Data sheet]. https://www.mouser.com/datasheet/2/678/avgo_s_a0002428009_1-2290947.pdf

Bať a, M., & Mikle, D. (2019). Battery management system hardware design for a student electric racing car. *IFAC-PapersOnLine*, *52*(27), 310–315. https://doi.org/10.1016/j.ifacol.2019.12.737

Birbir, Y., Yurtbasi, K., & Kanburoglu, V. (2019). Design of a single-phase SPWM inverter application with PIC microcontroller. *Engineering Science and Technology, an International Journal*, *22*(2), 592–599. https://doi.org/10.1016/j.jestch.2018.11.014

BorgWarner. (n.d.). *AC motor controller Gen5 Size 9 reference manual* [Manual]. Sevcon.

Brandstetter, P., & Kříček, T. (2012). Speed and current control of permanent magnet synchronous motor drive using IMC controllers. *Advances in Electrical and Computer Engineering*, *12*(4), 3–10. https://doi.org/10.4316/AECE.2012.0400

Davide, A. (2010). *Li-ion BMS: How much balancing current do you need?* [White paper]. Li-Ion BMS. https://liionbms.com/php/wp_balancecurrent.php

Dewan, S. B., & Straughen, A. (1975). *Power semiconductor circuits*. Wiley-Interscience.

Emadi, A., Lee, Y. J., & Rajashekara, K. (2008). Power electronics and motor drives in electric, hybrid electric, and plug-in hybrid electric vehicles. *IEEE Transactions on*

Industrial Electronics, 55(6), 2237–2245. https://doi.org/10.1109/TIE.2008.922768

Enepaq. (2023). *Li-ion building block with Sony/Murata VTC6: Battery module with temperature sensor* [Data sheet]. https://enepaq.com/wp-content/uploads/2023/09/VTC6-Sony-Murata-Li-ion-Battery-Module-With-Temperature-Sensor-Datasheet-Tesla-Battery-Sponsorship-Formula-SAE-Electric-Formula-Student-Battery-Pack.pdf

Formula SAE. (2022). *Formula SAE rules and series resources*. https://www.fsaeonline.com

Ghaderi, A., Umeno, T., & Sugai, M. (2016). An altered PWM scheme for single-mode seamless control of AC traction motors for electric drive vehicles. *IEEE Transactions on Industrial Electronics, 63*(3), 1385–1394. https://doi.org/10.1109/TIE.2015.2498901

Giri, F. (2013). *AC electric motors control: Advanced design techniques and applications*. Wiley.

Kamal, M. D. A., & Al-Fattah, J. (2025). The experimental study of an SPWM-based controller in an inverter. *Evolution in Electrical and Electronic Engineering, 6*(2), 446–456. https://doi.org/10.30880/eeee.2025.06.02.054penerbit.uthm.edu

Khalid, A. H., Rahman, M. M., & Amin, M. R. (2019). Effects of modulation index on harmonics of SP-PWM inverter-fed universal motor. *International Journal of Electrical and Computer Engineering, 9*(6), 5409–5419. https://doi.org/10.11591/ijece.v9i6.pp5409-5419

Krishna, G., Singh, R., Gehlot, A., Almogren, A., Altameem, A., Ur Rehman, A., & Hussen, S. (2024). Advanced battery management system enhancement using IoT and ML for predicting remaining useful life in Li-ion batteries. *Scientific Reports, 14*, Article 30394. https://doi.org/10.1038/s41598-024-80719-1

Liu, W., Placke, T., & Chau, K. T. (2022). Overview of batteries and battery management for electric vehicles. *Energy Reports, 8*, 4058–4084. https://doi.org/10.1016/j.egyr.2022.03.016

Lu, X., Chen, S., Wu, C., & Li, M. (2011). The pulse width modulation and its use in induction motor speed control. In *Proceedings of the 2011 Fourth International Symposium on Computational Intelligence and Design* (pp. 195–198). IEEE. https://doi.org/10.1109/ISCID.2011.150

Manandhar, D., Manandhar, N., & Phan, P. (2020). *Modular battery management system (BMS)* [Capstone technical report, University of Virginia]. https://libraetd.lib.virginia.edu/downloads/4q77fs08g

Microchip Technology. (2020). *ATmega48A/PA/88A/PA/168A/PA/328/P: megaAVR data sheet*. https://ww1.microchip.com/downloads/en/DeviceDoc/ATmega48A-PA-88A-PA-168A-PA-328-P-DS-DS40002061B.pdf

Mouser Electronics. (2020). *FGH60N60SFD IGBT: Field stop* [Data sheet]. https://www.mouser.mx/datasheet/2/308/1/FGH60N60SMD_D-2313587.pdf

Munsi, M. S., & Chaoui, H. (2024). Energy management systems for electric vehicles: A comprehensive review of technologies and trends. *IEEE Access, 12*, 55942–55972. https://doi.org/10.1109/ACCESS.2024.3371483

Nam, K. (2018). *AC motor control and electrical vehicle applications*. CRC Press.

Orion BMS. (2018). *Orion BMS 2 operational manual*. https://www.orionbms.com/manuals/pdf/OrionBMS2_OperationalManual.pdf

Palmas-Peláez, J. A., & García-Vite, P. (2013). Minimización de la distorsión armónica de una modulación PWM aplicada a un inversor conectado a la red eléctrica. *Revista Iberoamericana de Automática e Informática Industrial, 10*(2), 186–195. https://doi.org/10.1016/j.riai.2013.03.006

Patel, N., Bhoi, A. K., Padmanaban, S., & Holm-Nielsen, J. B. (Eds.). (2021). *Electric vehicles: Modern technologies and trends*. Springer. https://doi.org/10.1007/978-981-15-9251-5

Tamrakar, E., Patel, R., Kumar, A., Kumar Sahu, A., Ruchira, R. (2023). Experimental investigation and power quality analysis of solar micro-inverter for different operating conditions. *E3S Web of Conferences, 405*, Article 02024. https://doi.org/10.1051/e3sconf/202340502024

Texas Instruments. (2014). *xx555 precision timers* [Data sheet]. https://www.ti.com/lit/ds/symlink/se555.pdf

Texas Instruments. (2023). *OPA814 600-MHz, high-precision, unity-gain stable, FET-input operational amplifier* [Data sheet]. https://www.ti.com/lit/ds/symlink/opa814.pdf

UniTek Industrie Elektronik GmbH. (2012). *BAMOCAR-D3 digital battery-motor-controller manual*. https://www.unitek-industrie-elektronik.de

Victron Energy. (2020). *Lithium battery manual*. https://www.victronenergy.com/upload/documents/Lithium_Battery_Manual.pdf